ASTE Simultaneous HCN(4–3) and HCO$^+$(4–3) Observations of the Two Luminous Infrared Galaxies NGC 4418 and Arp 220

Masatoshi Imanishi *

National Astronomical Observatory, 2-21-1, Osawa, Mitaka, Tokyo 181-8588, Japan

masa.imanishi@nao.ac.jp

Kouichiro Nakanishi [†]

National Astronomical Observatory, 2-21-1, Osawa, Mitaka, Tokyo 181-8588, Japan

Masako Yamada

Institute of Astronomy and Astrophysics Academia Sinica, P.O. Box 23-141, Taipei 10617, Taiwan, R.O.C.

Yoichi Tamura

Nobeyama Radio Observatory, Minamimaki, Minamisaku, Nagano, 384-1305, Japan

and

Kotaro Kohno

Institute of Astronomy, University of Tokyo, 2-21-1, Osawa, Mitaka, Tokyo, 181-0015, Japan

Abstract

We report the results of HCN(J=4–3) and HCO$^+$(J=4–3) observations of two luminous infrared galaxies (LIRGs), NGC 4418 and Arp 220, made using the Atacama Submillimeter Telescope Experiment (ASTE). The ASTE wide-band correlator provided simultaneous observations of HCN(4–3) and HCO$^+$(4–3) lines, and a precise determination of their flux ratios. Both galaxies showed high HCN(4–3) to HCO$^+$(4–3) flux ratios of >2, possibly due to AGN-related phenomena. The $J = 4$–3 to $J = 1$–0 transition flux ratios for HCN (HCO$^+$) are similar to those expected for fully thermalized (sub-thermally excited) gas in both sources, in spite of HCN's higher critical density. If we assume collisional excitation and neglect an infrared radiative pumping process, our non-LTE analysis suggests that HCN traces gas with significantly higher density than HCO$^+$. In Arp 220, we separated the double-peaked HCN(4–3) emission into the eastern and western nuclei, based on velocity information. We confirmed that the eastern nucleus showed a higher HCN(4–3) to HCN(1–0) flux ratio, and thus contained a larger amount of highly excited molecular gas than the western nucleus.

Key words: galaxies: active — galaxies: nuclei — galaxies: ISM — radio lines:

1

galaxies — galaxies: individual (NGC 4418 and Arp 220)

1. Introduction

Luminous infrared galaxies (LIRGs) radiate the bulk of their large luminosities ($L \gtrsim 10^{11} L_{\odot}$) as infrared dust emission (Sanders & Mirabel 1996). Their large infrared luminosities indicate that (1) powerful energy sources are present, hidden behind dust; (2) energetic radiation from the hidden energy sources is absorbed by the surrounding dust; and (3) the heated dust grains re-emit this energy as infrared thermal radiation. To understand this LIRG population, it is essential to clarify the hidden energy sources, whether starbursts (i.e., nuclear fusion inside stars) are dominant, or active galactic nuclei (AGNs; active mass accretion onto a central compact supermassive black hole [SMBH] with $>10^6 M_{\odot}$) are also energetically important.

Unlike AGNs surrounded by a torus-shaped (toroidally-shaped) dusty medium, which are classified optically as Seyferts (Veilleux & Osterbrock 1987), LIRGs have a large amount of concentrated molecular gas and dust in their nuclei (Sanders & Mirabel 1996). For this reason, the putative compact AGNs can easily be *buried* (i.e., obscured in virtually all directions), making the optical detection of AGN signatures very difficult. However, investigating the energetic importance of such optically elusive *buried* AGNs is crucial to understand the true nature of the LIRG population.

A starburst (nuclear fusion) and a buried AGN (mass accretion onto a SMBH) have very different energy-generation mechanisms. Specifically, while UV is the predominant energetic radiation in a starburst, an AGN emits strong X-ray emission in addition to UV. The radiative energy generation efficiency of a nuclear fusion reaction in a normal starburst is only $\sim 0.5\%$ of Mc^2 (M is the mass of material used in the nuclear fusion reaction). Thus, the emission surface brightness of a starburst region is modest and has both observational (Werner et al. 1976; Soifer et al. 2000) and theoretical (Thompson et al. 2005) upper limits ($\sim 10^{13} L_{\odot}$ kpc^{-2}). An AGN, however, achieves high radiative energy generation efficiency (6–42% of Mc^2, where M is the mass of accreting material; Bardeen 1970; Thorne 1974), producing a very high emission surface brightness with $>10^{13} L_{\odot}$ kpc^{-2} (Soifer et al. 2000). These differences between a starburst and an AGN could create differences in the properties of the molecular gas and dust around the energy sources, allowing us to distinguish the hidden energy sources if, for example, different emission-line flux ratios are observed from the surrounding material.

Molecular gas emission lines in the sub-millimeter and millimeter wavelength ranges are

*   Department of Astronomy, School of Science, Graduate University for Advanced Studies (SOKENDAI), Mitaka, Tokyo 181-8588

†   Department of Astronomy, School of Science, Graduate University for Advanced Studies (SOKENDAI), Mitaka, Tokyo 181-8588

a potentially effective tool for probing this distinction, because the effects of dust extinction are so small in these wavelength ranges that signatures of AGNs deeply buried in gas and dust are detectable. It was found observationally that HCN(J=1–0) emission (rest frequency $\nu_{\rm rest}$ = 88.632 GHz or rest wavelength $\lambda_{\rm rest}$ = 3.385 mm) is systematically stronger, relative to HCO$^+$(J=1–0) ($\nu_{\rm rest}$ = 89.189 GHz or $\lambda_{\rm rest}$ = 3.364 mm), in AGN-dominated galaxy nuclei than in starburst galaxies (Kohno 2005; Krips et al. 2008). The trend of a strong HCN(1–0) to HCO$^+$(1–0) emission ratio was further confirmed in luminous buried AGN candidates (Imanishi et al. 2004; Imanishi et al. 2006b; Imanishi & Nakanishi 2006; Imanishi et al. 2007b; Imanishi et al. 2009). These results demonstrated that this HCN(1–0)/HCO$^+$(1–0) method functions as a diagnostic tool to distinguish the hidden energy sources of dusty galaxies. Extension to more distant, faint LIRGs is expected to play an important role for the comprehensive understanding of the LIRG population in the forthcoming Atacama Large Millimeter/submillimeter Array (ALMA) era. However, during the first operation phase of ALMA, band 3 (84–116 GHz or 2.59–3.57 mm) is the longest available wavelength coverage, so that this HCN(1–0)/HCO$^+$(1–0) method can be applied only to LIRGs at $z \leq 0.05$, hampering further systematic investigation of LIRGs. Energy diagnostic methods using other transition lines and/or other molecular species must be exploited.

HCN(J=4–3) ($\nu_{\rm rest}$ = 354.505 GHz) and HCO$^+$(4–3) ($\nu_{\rm rest}$ = 356.734 GHz) lines exist in Earth's 350 GHz atmospheric window, and can be one of the main frequency ranges exploited with ALMA. Because the frequency coverage of ALMA band 7 is 275–373 GHz, HCN(4–3) and HCO$^+$(4–3) lines can be studied in LIRGs at $z > 0.05$. Thus it is important to investigate whether AGNs show high HCN(4–3) to HCO$^+$(4–3) flux ratios, similar to the high HCN(1–0) to HCO$^+$(1–0) flux ratios.

In this paper, we present the results of simultaneous HCN(4–3) and HCO$^+$(4–3) observations of two nearby, well-studied LIRGs, NGC 4418 and Arp 220, both of which show high HCN(1–0) to HCO$^+$(1–0) flux ratios (Imanishi et al. 2004; Imanishi et al. 2007b). Throughout this paper, we adopt H$_0$ = 75 km s^{-1} Mpc^{-1}, $\Omega_{\rm M}$ = 0.3, and Ω_Λ = 0.7, to be consistent with our previously published papers.

2. Targets

NGC 4418, at z = 0.007, is a nearby LIRG with an infrared luminosity of L$_{\rm IR}$ $\sim$ 9 $\times$ 10^{10}L$_\odot$ (Table 1). Although it shows no clear Seyfert signature in the optical spectrum (Armus, Heckman, & Miley 1989; Lehnert & Heckman 1995), it is considered one of the closest and strongest buried AGN candidates, based on the AGN-like infrared spectral shape (Roche et al. 1991; Dudley & Wynn-Williams 1997; Spoon et al. 2001) and the high HCN(1–0) to HCO$^+$(1–0) flux ratio in the millimeter wavelength range (Imanishi et al. 2004).

Arp 220 (z = 0.018) is one of the best-studied nearby ultraluminous infrared galaxies (L$_{\rm IR}$ > 10^{12}L$_\odot$; Sanders et al. 1988). It has two nuclei, the eastern (Arp 220 E) and western

3

(Arp 220 W) nuclei, separated by $\sim 1''$ (Scoville et al. 2000; Soifer et al. 2000). The combined optical spectrum of both nuclei is classified as a LINER (i.e., non-Seyfert) (Veilleux et al. 1999). Starburst activity has been detected, but was energetically insufficient to account quantitatively for the observed infrared luminosity (Imanishi et al. 2006a; Armus et al. 2007; Imanishi et al. 2007a), indicating an energy source deeply buried in Arp 220's nuclear core (Spoon et al. 2004; Gonzalez-Alfonso et al. 2004). The energy source in Arp 220 W has a very high emission surface brightness, for which a buried AGN is a plausible (if not definite) explanation (Downes & Eckart 2007; Sakamoto et al. 2008).

3.   Observations and Data Reduction

The HCN(4–3) and HCO$^+$(4–3) observations of NGC 4418 and Arp 220 were made using the Wideband and High dispersion Spectrometer system with FFX correlator (WHSF) (Okuda & Iguchi 2008; Iguchi & Okuda 2008) on the Atacama Submillimeter Telescope Experiment (ASTE), a 10-m antenna located at Pampa La Bola in the Atacama Desert of Chile, at an altitude of 4800 m (Ezawa et al. 2004; Ezawa et al. 2008). Because the WHSF has 4-GHz frequency coverage in each side band, both the HCN(4–3) ($\nu_{\rm rest} = 354.505$ GHz) and HCO$^+$(4–3) ($\nu_{\rm rest} = 356.734$ GHz) lines were simultaneously observable. Figure 1 shows the raw ASTE WHSF spectra of NGC 4418 and Arp 220.

The observations were made in 2008 May, remotely from an ASTE operation room in the Mitaka campus of the National Astronomical Observatory of Japan, using the network observation system N-COSMOS3 developed by Kamazaki et al. (2005). Table 2 summarizes the detailed observation log. The weather conditions were excellent. Typical system temperatures were 180–300 K in the single side band. We employed the position-switching mode, so that the target position and off-sky position, 4 arcmin away from the target, were switched after each 10 s exposure. Telescope pointing was checked every 2 h. The total net on-source integration times were 200 min and 155 min for NGC 4418 and Arp 220, respectively. Flux calibration was made every observation day. By changing the frequency setting of the WHSF, we observed a strong emission line in W28 (IRC10216) at the frequency of the red-shifted HCN(4–3) and HCO$^+$(4–3) lines of NGC 4418 (Arp 220), to estimate the possible sensitivity variation along the WHSF bandpass. This variation was found to be <20%. The half-power beam width of the ASTE 10-m dish was 22$''$ at $\nu \sim 345$ GHz. At this frequency, the main beam efficiency is 0.6, and 1 K in antenna temperature corresponds to 78.5 Jy.

Data reduction was carried out with NEWSTAR, a package developed at Nobeyama Radio Observatory. A fraction of poor-quality data was flagged. To estimate the strength of HCN(4–3) and HCO$^+$(4–3) emission, we subtracted baselines from the obtained raw spectra. We first divided the spectra into two parts at the center, the lower-frequency HCN(4–3) part and higher-frequency HCO$^+$(4–3) part. The baseline was estimated independently in each part, based on the data points free from emission lines.

For NGC 4418, ten data sets with 20 min net on-source exposure time for each were obtained. The behavior of the baseline was extremely good, and the HCN(4–3) emission line was easily recognizable in individual data sets. First-order linear baselines were adopted both for the HCN(4–3) and HCO$^+$(4–3) emission lines, and the baseline-subtracted individual spectra were summed to obtain final spectra.

For Arp 220, final data consist of seven data sets with 20 min net on-source exposure and one data set with 15 min net on-source exposure. For the HCN(4–3) line, first-order linear baselines were adopted in individual data sets, and the baseline-subtracted individual spectra were summed. The HCN(4–3) emission line was detected in the final spectrum (see Appendix for more detail). Although we tried several baseline fits, the HCN(4–3) emission line was always visible, and its profile was virtually unchanged in the final spectrum, under reasonable baseline choices. For the HCO$^+$(4–3) line, when we applied a first-order linear baseline, winding patterns remained in the final spectrum, and HCO$^+$(4–3) line was not clearly detected. We thus attempted a second-order baseline, but the HCO$^+$(4–3) emission line remained undetected in the final spectrum.

4. Results

Figure 2 presents the final spectra around the HCN(4–3) and HCO$^+$(4–3) emission lines, after baseline subtraction. In both NGC 4418 and Arp 220, HCN(4–3) emission was clearly detected, with peak antenna temperatures of 7–15 mK, but HCO$^+$(4–3) emission was not. For NGC 4418, HCN(4–3) and HCO$^+$(4–3) emission line spectra are published here for the first time.

For NGC 4418, we fit the detected HCN(4–3) emission with a single Gaussian profile. For Arp 220 HCN(4–3) emission, a double-peaked profile was clearly seen. Thus we fit it with a two-component Gaussian profile. Table 3 summarizes the fitting results. The estimated HCN(4–3) fluxes were 220 Jy km s^{-1} and 410 Jy km s^{-1} for NGC 4418 and Arp 220, respectively, with the uncertainties of ∼20%. For the undetected HCO$^+$(4–3) emission, we adopted the lowest plausible continuum level in the spectra, and estimated conservative upper limits, by counting the possible flux excess above the adopted continuum levels. Table 3 summarizes these upper limits for the HCO$^+$(4–3) emission.

For Arp 220, HCN(4–3) measurements have been made previously by two groups (Wiedner et al. 2002; Greve et al. 2009). Our ASTE measurement of the HCN(4–3) flux (410±82 Jy km s^{-1}) fell between the previously reported values of 260 Jy km s^{-1} (Wiedner et al. 2002) and 587±118 Jy km s^{-1} (Greve et al. 2009). The velocity difference in the two components in the double-peaked HCN(4–3) profile was ∼300 km s^{-1} (Table 3), similar to that of HCN(1–0) emission (Imanishi et al. 2007b), further strengthening the detection of the HCN(4–3) emission line in Arp 220. Based on the argument of Imanishi et al. (2007b), we ascribe the lower-velocity (blue-shifted) and higher-velocity (red-shifted) components to the

Arp 220 W and E nuclei, respectively.

The HCN(4–3) to HCO$^+$(4–3) flux ratios [1] were >2.7 and >3.0 for NGC 4418 and Arp 220, respectively, where the ratio for Arp 220 used the combined emission from both nuclei. The non-detection of HCO$^+$(4–3) emission lines hampered the spectral separation into Arp 220 E and W and rendered independent estimates of the line flux ratio for these nuclear components difficult. HCN(4–3)/HCO$^+$(4–3) flux ratios significantly higher than unity were confirmed in both galaxies.

We emphasize that our simultaneous HCN(4–3) and HCO$^+$(4–3) observations using ASTE WHSF are crucial for obtaining reliable HCN(4–3) to HCO$^+$(4–3) flux ratios. Submillimeter and millimeter observations still present non-negligible uncertainties in absolute flux calibrations. In fact, even for measurements obtained in the last several years, the HCN(4–3) and HCN(1–0) fluxes of Arp 220 differed by a factor of 2 at maximum as observed by different groups with different telescopes under different weather conditions and using different calibration methods (Wiedner et al. 2002; Imanishi et al. 2007b; Gracia-Carpio et al. 2008; Greve et al. 2009). This level of absolute flux calibration uncertainty can be fatal to an investigation of the HCN(4–3) to HCO$^+$(4–3) flux ratios because we are discussing the difference of the ratios by about a factor of 2. By simultaneously observing HCN(4–3) and HCO$^+$(4–3) lines, the possible absolute flux calibration uncertainty does not propagate to the HCN(4–3)/HCO$^+$(4–3) flux ratios, which are then dominated only by statistical noises and fitting errors.

5. Discussion

5.1. HCN(4–3) to HCO$^+$(4–3) flux ratios

In this subsection, we explore HCN(4–3) and HCO$^+$(4–3) emission from NGC 4418 and Arp 220, in relation to HCN(1–0) and HCO$^+$(1–0). For this purpose, we used our ASTE WHSF and Nobeyama Millimeter Array (NMA) data (Imanishi et al. 2004; Imanishi et al. 2007b), because (1) simultaneous HCN and HCO$^+$ observations by both telescopes make the comparison of HCN to HCO$^+$ flux ratios reliable, and (2) HCN(1–0) and HCO$^+$(1–0) absolute fluxes in the NMA data have been confirmed to agree with measurements from other single-dish telescopes (Imanishi et al. 2004; Imanishi et al. 2007b). The NMA measurements of HCN(1–0) and HCO$^+$(1–0) fluxes are summarized in Table 4.

For NGC 4418, we obtained an HCN(4–3) to HCO$^+$(4–3) flux ratio > 2.7, confirming the high HCN to HCO$^+$ flux ratio previously found for the $J = 1$–0 transition line (~1.8; Imanishi et al. 2004). The HCN(4–3) to HCN(1–0) flux ratio was estimated to be 20. This is

---

[1]   By definition, flux is proportional to brightness-temperature × ν^2, where ν is frequency. Because HCN(4–3) ($\nu_{\rm rest}$ = 354.505 GHz) and HCO$^+$(4–3) ($\nu_{\rm rest}$ = 356.734 GHz) have very similar frequencies, their flux ratios are virtually identical to their brightness-temperature ratios. In this paper, we use a flux ratio.

comparable to the ν^2 scaling ($\sim$16) expected for fully thermalized optically thick gas (Riechers et al. 2006). The HCO$^+$(4–3) to HCO$^+$(1–0) flux ratio was <15.

For Arp 220, the HCN(4–3) and HCO$^+$(4–3) flux ratio was estimated to be >3.0. The $J = 4$–3 to $J = 1$–0 flux ratio for Arp 220 total emission was 12 and <8 for HCN and HCO$^+$, respectively. When we separated the emission from individual nuclei, the HCN(4–3) to HCN(1–0) flux ratios were 21 and 9 for Arp 220 E and W nuclei, respectively. The ratio is higher in Arp 220 E than Arp 220 W, further supporting the previous argument that a larger fraction of highly excited molecular gas is present in Arp 220 E (Greve et al. 2009).

The critical density of HCN is 2.3×10^5 cm^{-3} for $J = 1$–0 and 8.5×10^6 cm^{-3} for $J = 4$–3. That of HCO$^+$ is 3.4×10^4 cm^{-3} for $J = 1$–0, and 1.8×10^6 cm^{-3} for $J = 4$–3 (Table 3 of Greve et al. 2009). Because the critical density of HCO$^+$ is a factor of $\sim$5–7 smaller than HCN for both the $J = 1$–0 and $J = 4$–3 transitions, HCO$^+$ can be collisionally excited more easily than HCN in single-phase molecular gas. Thus, the stronger HCN emission in NGC 4418 and Arp 220 requires (1) an HCN abundance that is significantly higher than HCO$^+$, and/or (2) the presence of some physical mechanism that enhances HCN emission.

Regarding the first HCN abundance enhancement scenario, Yamada et al. (2007) concluded, based on three-dimensional line transfer simulations, that HCN abundance must be an order of magnitude higher than HCO$^+$ to account for the observed high HCN to HCO$^+$ flux ratio ($\sim$2). While the typical HCN to HCO$^+$ abundance ratio in our Galactic molecular cloud is $\sim$1 (Blake et al. 1987; Pratap et al. 1997; Dickens et al. 2000), HCN overabundance, relative to HCO$^+$, by an order of magnitude, is predicted in some parameter range for dense molecular gas illuminated by an X-ray emitting energy source (Meijerink & Spaans 2005). Since an AGN is a much stronger X-ray emitter than starbut activity, this HCN overabundance scenario is a possibility for the observed high HCN(4–3)/HCO$^+$(4–3) flux ratios in the buried AGN candidates, NGC 4418 and Arp 220.

Strong HCN emission in luminous buried AGN candidates may be explained by the infrared radiative pumping scenario (Aalto et al. 1995; Garcia-Burillo et al. 2006; Guelin et al. 2007; Weiss et al. 2007; Aalto et al. 2007a). In an AGN, the emission surface brightness is much higher than in a starburst, so that the surrounding dust is heated to a high temperature (several hundred K) and produces strong mid-infrared 10–20 μm continuum emission. The HCN molecule has a line at infrared 14.0 μm. Molecular gas around an AGN can be vibrationally excited by absorbing these infrared 14.0 μm photons, and through the subsequent cascade process, can enhance HCN rotational lines in the sub-millimeter and millimeter range.

Guelin et al. (2007) suggested that this infrared pumping scenario may work also for HCO$^+$ and HNC, because they have lines at 12.1 μm (HCO$^+$) and 21.7 μm (HNC). However, for this infrared pumping scenario to affect particular molecules, infrared photons at the wavelengths of these molecular lines must be absorbed. Namely, absorption features must be detected in infrared spectra at 14.0 μm (HCN), 12.1 μm (HCO$^+$), and 21.7 μm (HNC). While

the infrared HCN 14.0 μm absorption feature is clearly detected in highly obscured ultraluminous infrared galaxies, including NGC 4418 and Arp 220 (Lahuis et al. 2007; Veilleux et al. 2009), absorption features at HCO$^+$ 12.1 μm and HNC 21.7 μm are not (Veilleux et al. 2009). Therefore, we see observational signatures that this infrared radiative pumping scenario could be at work for HCN, but not for HCO$^+$ or HNC. This may explain the strong HCN emission found in luminous AGN candidates.

Since both the HCN overabundance and infrared radiative pumping scenarios could work more effectively in an AGN than starburst activity, the enhanced HCN(4–3) emission may originate in putative buried AGNs in NGC 4418 and Arp 220. Three-dimensional modelings which realistically incorporate actual physical parameters of molecular gas around an AGN are needed for more detailed quantitative comparison with observations.

5.2.   Molecular gas properties

For NGC 4418, the HCN(4–3) to HCN(1–0) flux ratio (20) was higher than the HCO$^+$(4–3) to HCO$^+$(1–0) flux ratio (<15). For Arp 220 as well, the former ratio (12) was higher than the latter ratio (<8). Thus, our ASTE observations suggest that $J = 4$–3 transition lines are excited more efficiently in HCN than HCO$^+$, in spite of the higher critical density of HCN(4–3) compared to HCO$^+$(4–3) (a factor of $\sim$5 [§5.1]). As mentioned in §5.1, in a single-phase molecular gas, molecular species with lower critical density are more easily collisionally excited. Thus, HCO$^+$ should be excited more than HCN. Some mechanisms are needed to explain the strong HCN(4–3) emission. Examples include a multiple phase molecular gas (Greve et al. 2009), and the infrared radiative pumping scenario. The second scenario will be investigated elsewhere, using a three-dimensional model (Yamada et al. 2009, in prep). Here, we explore the first possibility. Namely, we consider only collisional excitation and neglect the infrared radiative pumping process.

We used RADEX (van der Tak et al. 2007) to investigate molecular gas properties that could account for our ASTE and NMA results. The RADEX software adopts the non-LTE analysis of molecular line spectra, solving radiative transfer in simple geometry gas. We varied the H$_2$ number density and kinetic temperature from 10^3–10^8 cm^{-3} and 10–200 K, respectively. A uniform sphere with a line width of 200 km s^{-1} was assumed, based on the HCN(4–3) emission measurements (Table 3). X-ray observations suggested that both NGC 4418 and Arp 220 have highly-obscured, Compton thick ($N_H > 10^{24}$ cm^{-2}) AGNs (Maiolino et al. 2003; Iwasawa et al. 2005). Taking HCN and HCO$^+$ abundances relative to H$_2$ of 10^{-9}–10^{-8} (Blake et al. 1987; Dickens et al. 2000), column densities with 10^{16} cm^{-2} were adopted for both HCN and HCO$^+$. The T = 2.73 K background emission was also added for the calculation. Figure 3 shows the HCN(4–3) to HCN(1–0) and HCO$^+$(4–3) to HCO$^+$(1–0) flux ratios in Jy km s^{-1}, as a function of molecular gas number density and kinetic temperature. In the 10–200 K temperature range, the molecular gas number density was estimated to be $n_H > 10^6$ cm^{-3} to fit

8

the observed HCN(4–3) to HCN(1–0) flux ratios for NGC 4418 ($\sim$20) and Arp 220 ($\sim$12).

Now, the HCO$^+$(4–3) to HCO$^+$(1–0) flux ratios were <15 and <8 for NGC 4418 and Arp 220, respectively. For T > 25 K (>$10^{1.4}$ K), molecular gas with a number density n_H <10^6 cm^{-3} reproduced the observed HCO$^+$ flux ratios. Thus, assuming collisional excitation, we confirmed that in both NGC 4418 and Arp 220, HCN emission traces gas with a number density significantly higher than that traced by HCO$^+$ [2], as previously argued for Arp 220 based on the measurements of HCN(4–3), HCO$^+$(4–3), and other transition lines (Greve et al. 2009). Even given HCN and HCO$^+$ column densities of 10^{15} cm^{-2} and a line width of 300 km s^{-1}, our main conclusion is unchanged.

Three-dimensional hydrodynamic simulations of galactic disks have shown that the fraction of molecular gas with n_H > 10^6 cm^{-3} is miniscule (Wada & Norman 2007). Yet, the strong HCN(4–3) emission line detected in NGC 4418 and Arp 220 suggests the presence of a large amount of such high-density (n_H > 10^6 cm^{-3}) molecular gas, if the HCN(4–3) line is collisionally excited. It is likely that the high nuclear concentration of molecular gas in LIRGs increases the fraction of high-density molecular gas.

6. Summary

We presented the results of simultaneous HCN(4–3) and HCO$^+$(4–3) observations of two luminous infrared galaxies, NGC 4418 and Arp 220, using ASTE WHSF. Our main conclusions are as follows:

1. Strong HCN(4–3) emission was detected in both NGC 4418 and Arp 220, but HCO$^+$(4–3) emission provided only upper limits.
2. In both sources, we found HCN(4–3) to HCO$^+$(4–3) flux ratios of >2, even higher than the HCN(1–0) to HCO$^+$(1–0) emission line flux ratios. The high HCN/HCO$^+$ flux ratios could be explained by HCN overabundance and/or infrared radiative pumping scenarios, both of which may work more effectively in an AGN than starburst activity.
3. HCN(4–3) to HCN(1–0) flux ratios were higher than HCO$^+$(4–3) to HCO$^+$(1–0) flux ratios in both NGC 4418 and Arp 220, suggesting that higher J-transitions were excited more efficiently in HCN than HCO$^+$. If we neglect an infrared radiative pumping mechanism, and consider only collisional excitation, these results are incompatible with a one-zone molecular gas model, because the critical density of HCN is higher than HCO$^+$ at these transitions. A multi-phase molecular gas in which HCN selectively probes higher-density molecular gas than HCO$^+$ is required. We applied RADEX models, and found that in both NGC 4418 and Arp 220, gas with a number density n_H > 10^6 cm^{-3} and n_H < 10^6

---

[2] For NGC 4418, the small HCN(3–2) to HCO$^+$(3–2) flux ratio (less than unity) reported by Aalto et al. (2007b) is not compatible with our model. The HCN(3–2) flux itself is also significantly lower than that expected for thermalized, optically thick gas. We have no clear interpretation, as long as only collisional excitation is considered.

cm^{-3} reproduced the observed HCN and HCO$^+$ $J = 4$–3 to 1–0 flux ratios, respectively, in the 25–200 K temperature range.

4. For Arp 220, HCN(4–3) to HCN(1–0) flux ratio is higher in Arp 220 E than in Arp 220 W, suggesting that Arp 220 E contains a larger amount of highly excited molecular gas.

Appendix 1.   Analysis of the Arp 220 HCN(4–3) emission line

We explain in detail how the HCN(4–3) emission line of Arp 220 becomes detectable in our analysis. We took eight independent data sets. Single-order linear baselines were employed in individual data sets (Figure 4) and eight baseline-subtracted spectra were summed to obtain a final HCN(4–3) spectrum. The HCN(4–3) emission was clearly detected in the final spectrum of Arp 220, as seen in Figure 2.

References

Aalto, S., Booth, R. S., Black, J. H., & Johansson, L. E. B. 1995, A&A, 300, 369

Aalto, S., Spaans, M., Wiedner, M. C., & Huttemeister, S. 2007a, A&A, 464, 193

Aalto, S., Monje, R., & Martin, S. 2007b, A&A, 475, 479

Armus, L., Heckman, T. M., & Miley, G. K. 1989, ApJ, 347, 727

Armus, L., et al. 2007, ApJ, 656, 148

Bardeen, J. M. 1970, Nature, 226, 64

Blake, G. A., Sutton, E. C., & Masson, C. R., & Phillips, T. G. 1987, ApJ, 315, 621

Dickens, J. E., Irvine, W. M., Snell, R. L., Bergin, E. A., Schloerb, F. P., Pratap, P., & Miralles, M. P. 2000, ApJ, 542, 870

Downes, D., & Eckart, A. 2007, A&A, 468, L57

Dudley, C. C., & Wynn-Williams, C. G. 1997, ApJ, 488, 720

Ezawa, H. et al. 2004, Proc. SPIE, 5489, 763

Ezawa, H. et al. 2008, Proc. SPIE, 7012, 6

Garcia-Burillo, S., et al. 2006, ApJ, 645, L17

Gonzalez-Alfonso, E., Smith, H. A., Fischer, J., & Cernicharo, J., 2004, ApJ, 613, 247

Gracia-Carpio, J., Garcia-Burillo, S, Planesas, P., Fuente, A., & Usero, A. 2008, A&A, 479, 703

Greve, T. R., Papadopoulos, P. P., Gao, Y., & Radford, S. J. E. 2009, ApJ, 692, 1432

Guelin, M., et al. 2007, A&A, 462, L45

Iguchi, S., & Okuda, T. 2008, PASJ, 60, 857

Imanishi, M., Dudley, C. C., & Maloney, P. R. 2006a, ApJ, 637, 114

Imanishi, M., Dudley, C. C., Maiolino, R., Maloney, P. R., Nakagawa, T., & Risaliti, G. 2007a, ApJS, 171, 72

Imanishi, M., & Nakanishi, K. 2006, PASJ, 58, 813

Imanishi, M., Nakanishi, K., Kuno, N., & Kohno, K. 2004, AJ, 128, 2037

Imanishi, M., Nakanishi, K., & Kohno, K. 2006b, AJ, 131, 2888

Imanishi, M., Nakanishi, K., Tamura, Y., Oi, N., & Kohno, K. 2007b, AJ, 134, 2366

Imanishi, M., Nakanishi, K., Tamura, Y., & Peng, C. -H. 2009, AJ, 137, 3581

Iwasawa, K., Sanders, D. B., Evans, A. S., Trentham, N., Miniutti, G., & Spoon, H. W. W. 2005, MNRAS, 357, 565

Kamazaki, T., et al. 2005, Astronomical Society of the Pacific Conference Series, 347, 533

Kohno, K. 2005, in AIP Conf. Ser. 783, The Evolution of Starbursts, ed. S. Hüttemeister, E. Manthey, D. Bomans, & K. Weis (New York: AIP), 203 (astro-ph/0508420)

Krips, M., Neri, R., Garcia-Burillo, S., Martin, S., Combes, F., Gracia-Carpio, J., & Eckart, A. 2008, ApJ, 677, 262

Lahuis, F. et al. 2007, ApJ, 659, 296

Lehnert, M. D., & Heckman, T. M. 1995, ApJS, 97, 89

Maiolino, R. et al. 2003, MNRAS, 344, L59

Meijerink, R., & Spaans, M. 2005, A&A, 436, 397

Okuda, T., & Iguchi, S. 2008, PASJ, 60, 315

Pratap, P., Dickens, J. E., Snell, R. L., Miralles, M. P., Bergin, E. A., Irvine, W. M., & Schloerb, F. P. 1997, ApJ, 486, 862

Riechers, D. et al. 2006, ApJ, 650, 604

Roche, P. F., Aitken, D. K., Smith, C. H., & Ward, M. J. 1991, MNRAS, 248, 606

Sakamoto, K. et al. 2008, ApJ, 684, 957

Sakamoto, K. et al. 2009, ApJ, 700, L104

Sanders, D. B., & Mirabel, I. F. 1996, ARA&A, 34, 749

Scoville, N. Z. et al. 2000, AJ, 119, 991

Soifer, B. T. et al. 2000, AJ, 119, 509

Spoon, H. W. W., Keane, J. V., Tielens, A. G. G. M., Lutz, D., & Moorwood, A. F. M. 2001, A&A, 365, L353

Spoon, H. W. W., Moorwood, A. F. M., Lutz, D., Tielens, A. G. G. M., Siebenmorgen, R., & Keane, J. V. 2004, A&A, 414, 873

Thompson, T. A., Quataert, E., & Murray, N. 2005, ApJ, 630, 167

Thorne, K. S. 1974, ApJ, 191, 507

van der Tak, F. F. S., Black, J. H., Schoier, F. L., Jansen, D. J., & van Dishoeck, E. F. 2007, A&A, 468, 627

Veilleux, S., Kim, D. -C., & Sanders, D. B. 1999, ApJ, 522, 113

Veilleux, S., & Osterbrock, D. E. 1987, ApJS, 63, 295

Veilleux, S., et al. 2009, ApJS, 182, 628

Wada, K., & Norman, C. 2007, ApJ, 660, 276

Wang, Y., Jaffe, D. T., Graf, U. U., & Evans II, N. J. 1994, ApJS, 95, 503

Weiss, A., Downes, D., Neri, R., Walter, F., Henkel, C., Wilner, D. J., Wagg, J., & Wiklind, T. 2007, A&A, 467, 955

Werner, M. W., Gatley, I., Harper, D. A., Becklin, E. E., Loewenstein, R. F., Telesco, C. M., & Thronson, H. A. 1976, ApJ, 204, 420

Wiedner, M. C., Wilson, C. D., Harrison, A., Hills, R. E., Lay, O. P., & Carlstrom, J. E., 2002, ApJ, 581, 299

Yamada, M., Wada, K., & Tomisaka, K. 2007, ApJ, 671, 73

Table 1. Detailed information on the observed LIRGs

Object	Redshift	f_{12}	f_{25}	f_{60}	f_{100}	$\log L_{\mathrm{IR}}$ ($\log L_{\mathrm{IR}}/L_{\odot}$)
		(Jy)	(Jy)	(Jy)	(Jy)	(ergs s^{-1})
(1)	(2)	(3)	(4)	(5)	(6)	(7)
NGC 4418	0.007 [a]	0.9	9.3	40.7	32.8	44.5 (10.9)
Arp 220	0.018 [b]	0.48	7.92	103.33	112.40	45.7 (12.1)

Notes.

Col.(1): Object name.

Col.(2): Redshift.

Cols.(3)–(6): f_{12}, f_{25}, f_{60}, and f_{100} are *IRAS FSC* fluxes at 12, 25, 60, and 100 μm, respectively.

Col.(7): Decimal logarithm of the infrared $(8-1000\ \mu\mathrm{m})$ luminosity in ergs s^{-1} calculated as follows: $L_{\mathrm{IR}} = 2.1 \times 10^{39} \times \mathrm{D(Mpc)}^2 \times (13.48 \times f_{12} + 5.16 \times f_{25} + 2.58 \times f_{60} + f_{100})$ ergs s^{-1} (Sanders & Mirabel 1996). The values in parentheses are the decimal logarithms of the infrared luminosities in units of solar luminosities.

[a]: 1 arcsec corresponds to 130 pc.

[b]: 1 arcsec corresponds to 340 pc.

Table 2. Observing log of ASTE observations

Object	Observing Date	Central	Pointing	Flux
	(UT)	frequency	calibrator	calibrator
(1)	(2)	(3)	(4)	(5)
NGC 4418	2008 May 22, 23, 24, 27	353.15	V Hya, IRC10216	W28
Arp 220	2008 May 24, 27	349.21	RX Boo	IRC10216

Notes.

Col.(1): Object name.

Col.(2): Observation date in UT.

Col.(3): Central frequency of ASTE WHSF used for the observations.

Col.(4): Pointing calibrator object name.

Col.(5): Flux calibrator object name.

Table 3. Properties of HCN(4–3) and HCO$^+$(4–3) emission lines

Object	Line	LSR velocity [km s^{-1}]	Line width [km s^{-1}]	Flux [K km s^{-1}]	Flux [Jy km s^{-1}]	Luminosity 10^7 [K km s^{-1} pc^2]	Ratio
(1)	(2)	(3)	(4)	(5)	(6)	(7)	(8)
NGC 4418	HCN(4–3)	2060	335	4.7	220	4.7	>2.7
	HCO$^+$(4–3)	—	—	<1.7	<80	<1.7	
Arp 220	HCN(4–3)	5265, 5560	220,200	8.7	410	57	>3.0
				3.4 (W) + 5.3 (E)	160 (W) + 250 (E)	22 (W) + 35 (E)	
	HCO$^+$(4–3)	—	—	<2.9	<135	<19	

Notes.

Col.(1): Object name.

Col.(2): HCN(4–3) or HCO$^+$(4–3) line.

Col.(3): LSR velocity $\{v_{opt} \equiv (\frac{\nu_0}{\nu} - 1) \times c\}$ of the HCN(4–3) and HCO$^+$(4–3) in [km s^{-1}].

Col.(4): Line width in FWHM of the HCN(4–3) and HCO$^+$(4–3) emission lines in [km s^{-1}].

Col.(5): Flux of the HCN(4–3) and HCO$^+$(4–3) emission lines in main beam temperature in [K km s^{-1}]. For ASTE, the main beam efficiency is $\eta \sim 0.6$ at $\nu \sim 345$ GHz. For the HCN(4–3) line of Arp 220, individual contributions from Arp 220 E and W are also shown. The flux uncertainty is estimated to be <20%, based on the combination of the empirical one of ASTE WHSF (10–15%) and systematic one of flux calibrators ($\sim$10%) (Wang et al. 1994).

Col.(6): Flux of the HCN(4–3) and HCO$^+$(4–3) emission lines in [Jy km s^{-1}]. For ASTE, 1 [K] in main beam temperature corresponds to 47 [Jy] at $\nu \sim 345$ GHz.

Col.(7): Luminosity of the HCN(4–3) and HCO$^+$(4–3) emission lines in $\times 10^7$[K km s^{-1} pc^2].

Col.(8): HCN(4–3)/HCO$^+$(4–3) flux ratio (flux $\propto \nu^2 \times$ brightness-temperature). Because both the HCN(4–3) and HCO$^+$(4–3) data are taken simultaneously, the ratio is not affected by possible absolute flux calibration uncertainties in the ASTE observations (see §4).

Table 4. HCN and HCO$^+$ data at $J = 4$–3 and $J = 1$–0 transition lines for NGC 4418 and Arp 220

Object	Line	Flux	Reference
(1)	(2)	(3)	(4)
NGC 4418	HCN(4–3)	220±44	This work
	HCO$^+$(4–3)	<80	This work
	HCN(1–0)	10.3	Imanishi et al. (2004)
	HCO$^+$(1–0)	5.5	Imanishi et al. (2004)
Arp 220	HCN(4–3)	410±82	This work
		250 (E), 160 (W)	This work
		260	Wiedner et al. (2002)
		587±118	Greve et al. (2009)
	HCO$^+$(4–3)	<135	This work
		106±23	Greve et al. (2009)
		80	Sakamoto et al. (2009)
	HCN(1–0)	34	Imanishi et al. (2007b)
		12 (E), 18 (W)	Imanishi et al. (2007b)
	HCO$^+$(1–0)	18	Imanishi et al. (2007b)
		5.5 (E), 6.5 (W)	Imanishi et al. (2007b)

Notes.

Col.(1): Object name.

Col.(2): HCN or HCO$^+$ line.

Col.(3): Flux in [Jy km s^{-1}]. For Arp 220, individual fluxes from Arp 220 E and W are also shown. For HCN(1–0) and HCO$^+$(1–0) fluxes from Arp 220 E and W, only the spatially unresolved core emission is extracted.

Col.(4): Reference.
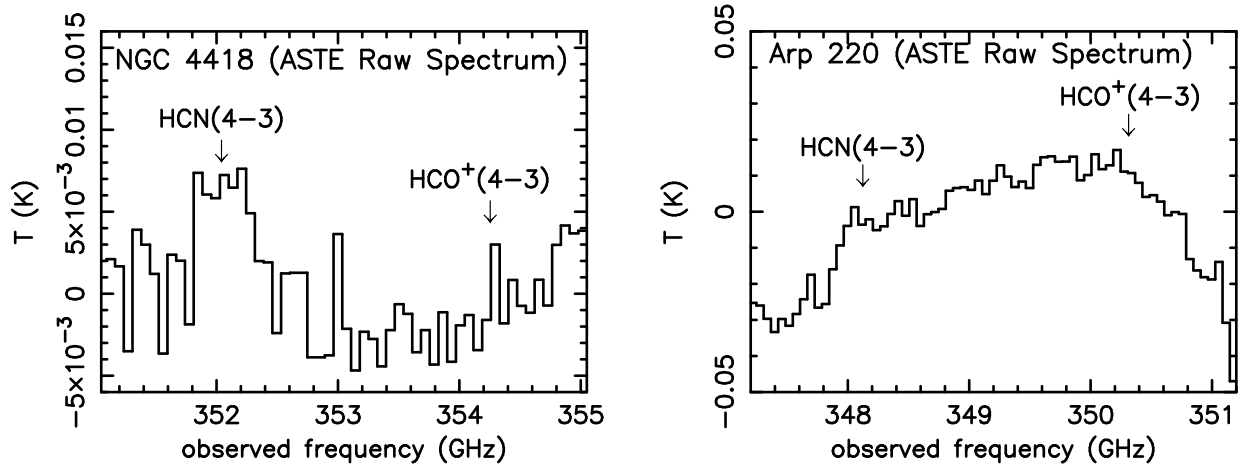
Fig. 1. ASTE WHSF wide-band (4 GHz) spectra of NGC 4418 and Arp 220, before baseline subtraction. The abscissa is observed frequency in [GHz] and the ordinate is antenna temperature in [K]. The spectrum is smoothed to a velocity resolution of 60 km s^{-1} and 50 km s^{-1} for NGC 4418 and Arp 220, respectively. The expected frequency of the HCN(4–3) and HCO$^+$(4–3) lines are indicated as arrows. HCN(4–3) and HCO$^+$(4–3) emission lines are simultaneously covered.
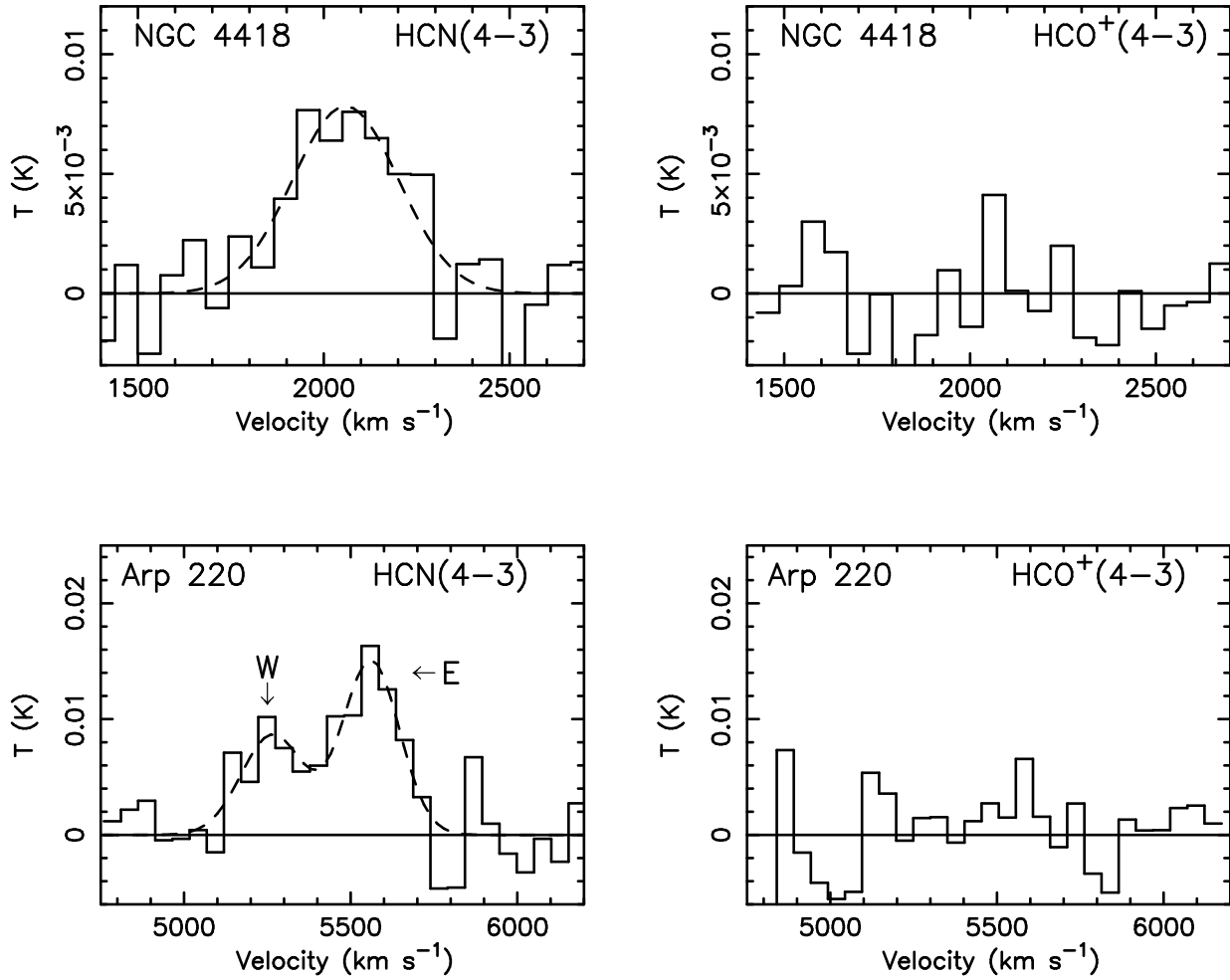
Fig. 2. HCN(4–3) and HCO$^+$(4–3) spectra of NGC 4418 and Arp 220, after baseline subtraction. First-order linear fits were basically adopted as the baselines, except for the Arp 220 HCO$^+$(4–3) line, for which a second-order fit was employed. The abscissa is velocity in [km s^{-1}] and the ordinate is antenna temperature in [K]. Spectra of NGC 4418 and Arp 220 are smoothed to velocity resolutions of 60 km s^{-1} and 50 km s^{-1}, respectively. Gaussian fits are over-plotted as dashed lines for the detected HCN(4–3) lines in NGC 4418 and Arp 220. For the Arp 220 HCN(4–3) line, we ascribe the blue (lower velocity) and red (higher velocity) components to Arp 220 W (denoted as "W") and Arp 220 E ("E"), respectively, based on Nobeyama Millimeter Array interferometric HCN(1–0) and HCO$^+$(1–0) data (Imanishi et al. 2007b) (see §4). The horizontal solid line indicates the zero flux level.
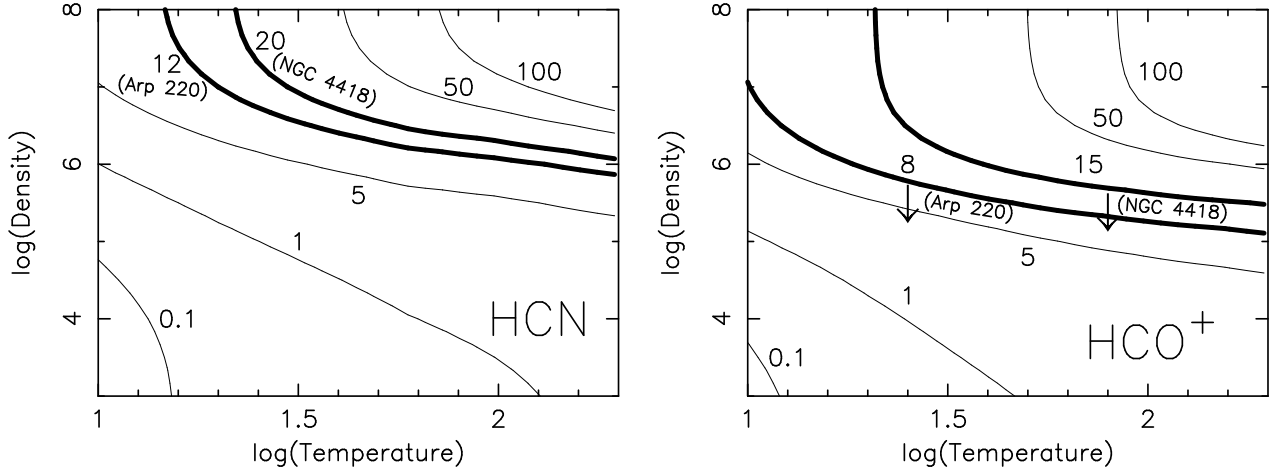
Fig. 3. HCN(4–3) to HCN(1–0) (*Left*) and HCO$^+$(4–3) to HCO$^+$(1–0) (*Right*) flux ratios in [Jy km s^{-1}] as a function of gas number density and kinetic temperature, calculated with RADEX. The abscissa and ordinate are the decimal logarithms of kinetic temperature in [K] and H$_2$ gas number density in [cm^{-3}], respectively. The HCN and HCO$^+$ column density is assumed to be 10^{16} cm^{-2} (see §5.2). A velocity width of 200 km s^{-1} was adopted (see §5.2). Contours are 0.1, 1, 5, 12, 20, 50, and 100 for HCN, and 0.1, 1, 5, 8, 15, 50, and 100 for HCO$^+$. The measured ratios for NGC 4418 and Arp 220 are indicated as thick lines. In the calculated parameter range, the line optical depth is 0–100 (i.e., reliable range in RADEX calculations).
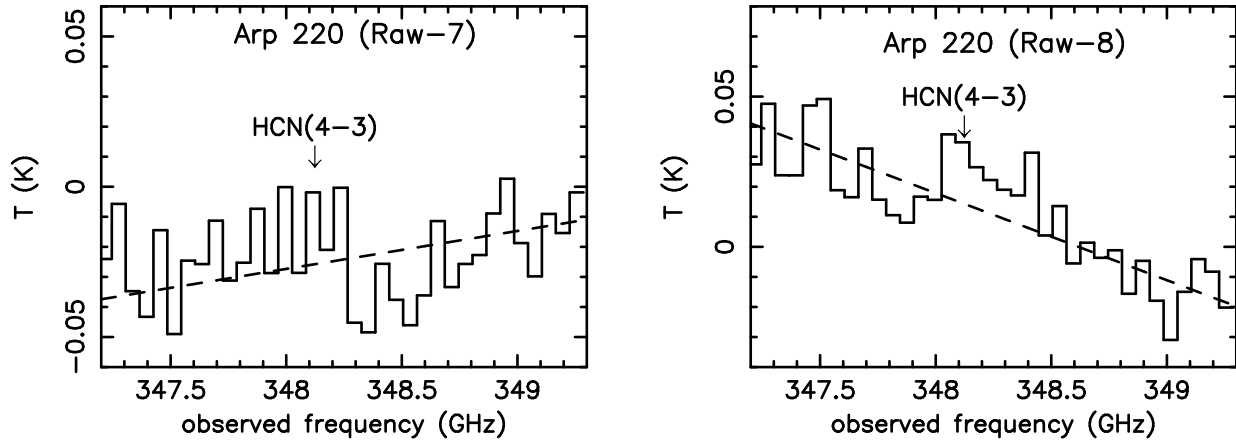
19
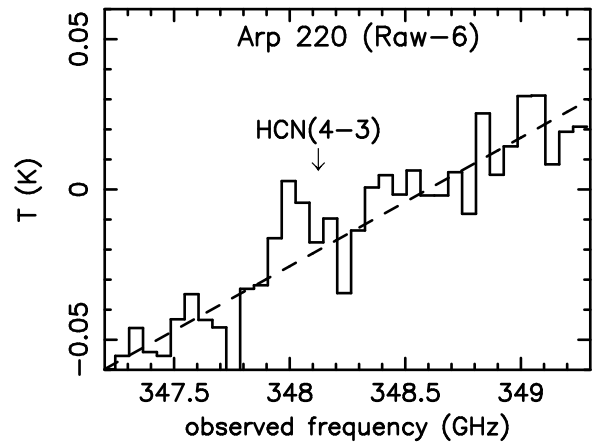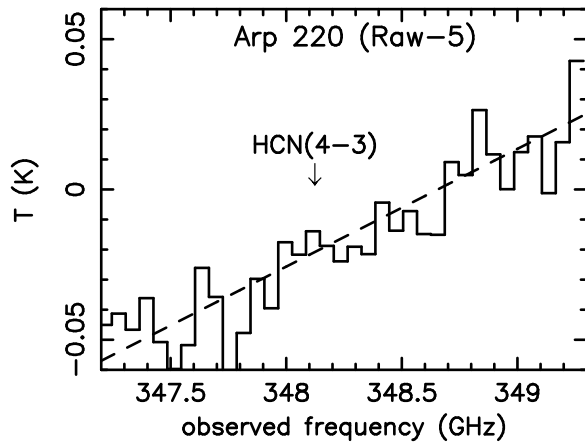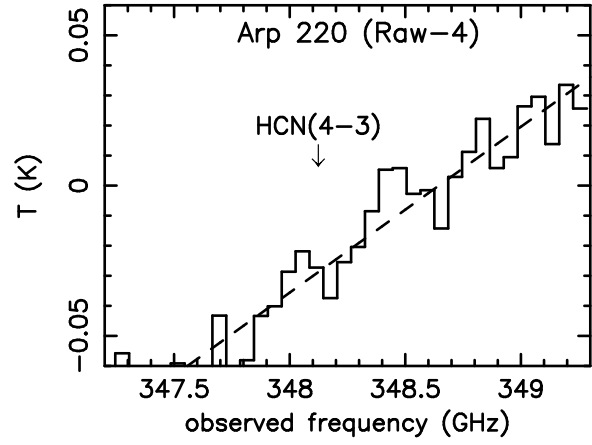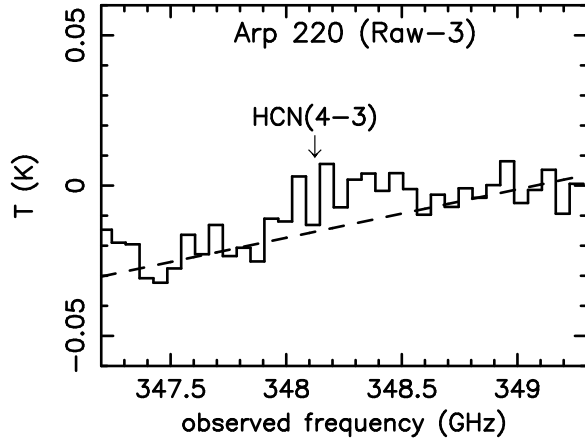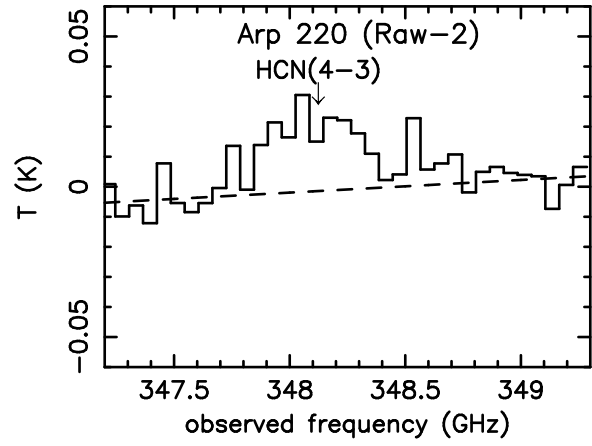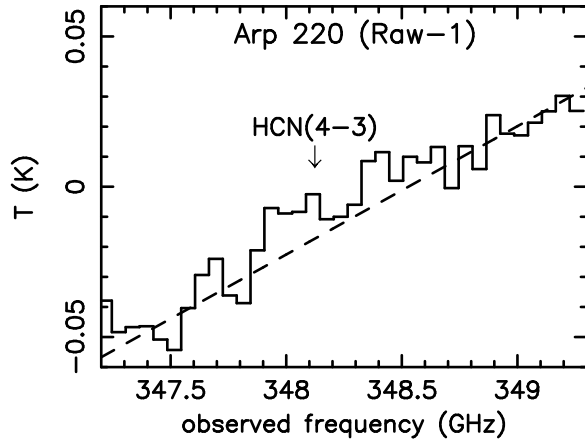
Fig. 4. Adopted linear baseline fits for individual unbinned HCN(4–3) spectra of Arp 220 (dashed lines), and smoothed spectra with velocity resolutions of 50 km s^{-1} (solid lines). Signatures of the HCN(4–3) emission lines are seen in most of the individual spectra.